



Effect of pattern geometry on bubble dynamics and heat transfer on biphilic surfaces

Pedro Pontes^a, Ricardo Cautela^a, Emanuele Teodori^b, Ana Moita^{a,*}, Yan Liu^c, A.L.N. Moreira^a, Artem Nikulin^d, Elena Palomo del Barrio^{d,e}

^a IN+ Center for Innovation, Technology and Policy Research, Instituto Superior Técnico, Av. Rovisco Pais, 1049-001 Lisboa, Portugal

^b ASML Holding N.V., De Run 6501, 5504 DR Veldhoven, The Netherlands

^c Key Laboratory of Engineering Bionics, Jilin University, Changchun 130022, China

^d Centre for Cooperative Research on Alternative Energies (CIC energiGUNE), Basque Research and Technology Alliance (BRTA), Alava Technology Park, Albert Einstein 48, 01510 Vitoria-Gasteiz, Spain

^e Ikerbasque — Basque Foundation for Science, María Díaz Haroko 3, 48013 Bilbao, Spain

ARTICLE INFO

Keywords:

Thermography
Wettability
Biphilic surfaces
Bubble dynamics
Pool boiling
Heat transfer

ABSTRACT

Recognizing the relevance of wettability in pool boiling heat transfer, few authors have reported significantly enhanced heat transfer coefficients using the so-called biphilic surfaces, i.e. hydrophilic surfaces with hydrophobic regions. However, the development of these patterns is still scarcely reported in the literature and many studies rely on a trial and error approach. In this context, the present work addresses a systematic analysis of the effect of the geometry of biphilic patterns on bubble dynamics and consequently on the heat transfer processes occurring in pool boiling. Geometric representative quantities such as the size of the superhydrophobic regions and their relative position are systematically varied and their effect is analyzed in detail in both bubble dynamics and heat transfer processes, using synchronized high-speed video and time-resolved thermography. The results show that the size of the superhydrophobic regions affects bubble dynamics and the rate of evaporated mass, thus influencing the heat flux term associated to the latent heat of evaporation. In this context, patterns with smaller superhydrophobic areas are the most effective at removing heat through evaporation. Regarding the distance between the superhydrophobic areas, the results support the use of the minimum distance between superhydrophobic areas, that is, in the limit to promote coalescence. For this distance there is still no significant interaction between the bubbles sites, but the controlled coalescence promotes the occurrence of a periodic induced flow between the superhydrophobic regions, which contributes to cool the surface. Also, heat flux calculations confirm that heat flux peaks coincide with bubble departure occurrences in the superhydrophobic areas, thus confirming the heat transfer enhancement promoted by this kind of surfaces.

1. Introduction

In spite of the paramount role of wettability in nucleation and bubble dynamics, which consequently affects pool boiling heat transfer, a clear and explicit quantification of this effect is not yet presented in the open literature Malavasi et al. [8]. Strategies to enhance pool boiling heat transfer often rely on changing the surface topography in a trial and error approach, based on measurements of the heat transfer coefficient (HTC) and of the critical heat flux (CHF) Kim et al. [6] and only more recent studies reinforce the need to follow a more systematic approach Teodori et al. [18], Moita et al. [9], Buongiorno et al. [2]. Alternatively, a few authors report a significant improve in pool boiling heat transfer coefficients, using surfaces composed by patterns of

hydrophobic/superhydrophobic micro-regions in hydrophilic/superhydrophilic substrates, the so-called biphilic surfaces. In this context, Betz et al. [1] report enhanced values for the heat transfer coefficients when using biphilic surfaces, which were attributed to the fact that the hydrophobic (and superhydrophobic) regions promoted nucleation at very low superheat values, thus increasing the number of active nucleation sites, while the hydrophilic (and superhydrophilic) area around the hydrophobic regions would prevent bubbles from growing too big, coalesce and form an insulating vapour blanket. Jo et al. [5] also reports higher heat transfer coefficients for biphilic surfaces, when compared to smooth hydrophilic surfaces. After testing different patterns, in an empirical approach, Jo et al. [5] refer that the highest values of the heat transfer coefficient were obtained with biphilic patterns composed

* Corresponding author.

E-mail address: anamoita@tecnico.ulisboa.pt (A. Moita).

<https://doi.org/10.1016/j.expthermflusci.2020.110088>

Received 15 November 2019; Received in revised form 8 February 2020; Accepted 16 February 2020

Available online 20 February 2020

0894-1777/ © 2020 Elsevier Inc. All rights reserved.

Nomenclature*Alphabetic*

A	area of superhydrophobic region, [cm ²]
c_p	specific heat, [J/(kg K)]
d_{spot}	distance separating superhydrophobic areas, [mm]
e	relative error [%]
f	frequency of bubble detachment, [Hz]
I	current fed to the stainless steel foil, [A]
k	conductivity, [W/(m K)]
m'_{evap}	evaporated mass flux, [kg/s]
q''	heat flux, [W/cm ²] or [W/m ²]
R	mean roughness, [μm]
T	fluid temperature, [°C]

Other Symbols

$\Delta\theta$	contact angle hysteresis, [°]
δ	thickness, [m]
\varnothing	superhydrophobic area diameter, [mm]
ρ	density, [kg/m ³]
θ	contact angle, [°]

Subscripts

a, r, s	advancing, receding and static (contact angle)
a, z	average, peak-peak (roughness)
$evap$	evaporated water
h	foil heater
sat	saturation temperature
$spot$	superhydrophobic area

by nine hydrophobic regions of 1 mm in diameter. However, the critical heat flux obtained with these biphilic surfaces was lower than that evaluated for the bare hydrophilic surfaces. In a subsequent work, Jo et al. [3] try to explain the CHF values obtained with the biphilic surfaces, arguing that the CHF is more dependent on the area ratio between hydrophobic regions and the hydrophilic substrate than on the area of the hydrophobic regions and/or of the distance between them. Lately other studies have explored heat transfer enhancement with biphilic surfaces such as Kumar et al. [7]. Other authors such as Motezakker et al. [11] have tried to prove the dependence of CHF and heat transfer on the area ratio, achieving an optimal configuration through several iterations. Despite these encouraging results, a systematic approach towards the development of such patterns based on the physics governing the boiling mechanisms is still scarcely reported. In this context, a few authors argue for the vital role of bubble dynamics in an efficient process to devise complex surfaces in a more systematic way (e.g. [18,2,4]), Yamada et al. [19]. In this context, Sadaghiani et al. [15] explain some of the phenomena that occur during pool boiling and how bubble dynamics, namely coalescence can be related to pool boiling heat transfer. Also, Zupančič et al. [20] use thermographic and high-speed images to compare bubble dynamics on structured, PDMS coated and bare stainless steel foils. Although thermographic and high-speed images were not synchronized, Zupančič et al. [20] could link bubble detachment with some thermal events occurring at the interface. This technique allowed the authors to observe the main difference in thermal dissipation during nucleation for the several types of surfaces analyzed. However, and even with the relevant contribution of these few aforementioned studies, literature still lacks an accurate description of the fundamental phenomena occurring during bubble generation and detachment on biphilic patterns, particularly the intricate relation between bubble dynamics and heat transfer, which actually governs the whole boiling curve behaviour at the macroscopic level, e.g. Teodori et al. [18], Buongiorno et al. [2], Malavasi et al. [8].

Within this scope and following our previous work Teodori et al. [18], the present study concerns the detailed characterization of bubble dynamics on biphilic surfaces towards the development of an optimum biphilic pattern, to enhance pool boiling heat transfer at reduced surface superheat. The analysis covers the detailed characterization of bubble dynamics and heat flux, synchronizing high-speed video with time resolved thermography. The geometrical conditions are studied, from a single bubble to a small array of 2 and 3 hydrophobic regions, where the size of the hydrophobic region, distance between regions and relative position are systematically varied, to infer on their influence on bubble dynamics and to characterize possible bubble and nucleation sites interaction. These effects are also observed when characterizing the heat flux terms and describing the flow that may be induced by the

interaction between superhydrophobic regions (which act as nucleation sites).

2. Experimental setup and procedures

2.1. Experimental setup

In order to perform experimental tests in pool boiling conditions a setup was assembled. This temperature-controlled system was equipped with high-speed and thermal imaging, that enabled bubble dynamic analysis and heat transfer characterization. Fig. 1 shows, in a schematic way, the essential components responsible for the general operation of the experimental setup.

The core component to consider is the main tank (10), which is filled with pre-heated and degassed distilled water by the degassing station (1). The water is maintained at the saturation temperature with the aid of two electrical resistances, a PID controlled cartridge heater and a coil heater.

Considering that the tank is an open system, a tube has been placed on its top (5) in order to redirect the generated water vapor to a container (4), where it condenses. The distilled water flows out of the degassing station into the tank via a tube (7), which is covered by an insulating sleeve and controlled by a valve (2).

Two K type thermocouples and an OMEGA DYNE INC pressure transducer (6) are used to control the working conditions inside the main tank, which are constantly monitored during the use of the experimental setup. The information taken from these sensors is sent through two data readers (DAQ 1 and 2) to a computer (PC 1).

The biphilic surfaces are accommodated at the base of the tank. These surfaces are made from stainless-steel (AISI304) and are heated by Joule effect when fed by a HP6274B DC Power Supply (8), to promote a controlled nucleate boiling. Bubble dynamics phenomena are recorded by a Phantom v4.2 high-speed camera (Camera 1), which has an optical access to the tank through one of the tank's windows. In the opposite window a LED (3) is mounted, which illuminates the interior of the tank. Index 9 represents the electrical cables that are linked to the connectors of the tank's base and transmit the electric current.

The test biphilic surfaces have an electrical resistance of 0.052 Ω and a very reduced thickness of 20 μm, so that a Onca MWIR-InSb-320 high-speed IR camera (Camera 2), mounted underneath them, can capture thermographic images of the surface temperature variation. The surface thickness was selected after some test trials and following the recommendations of Sielaff, Dietl, Herbert and Stephan [16]. The images captured by both cameras are viewed in real time on a second computer (PC 2).

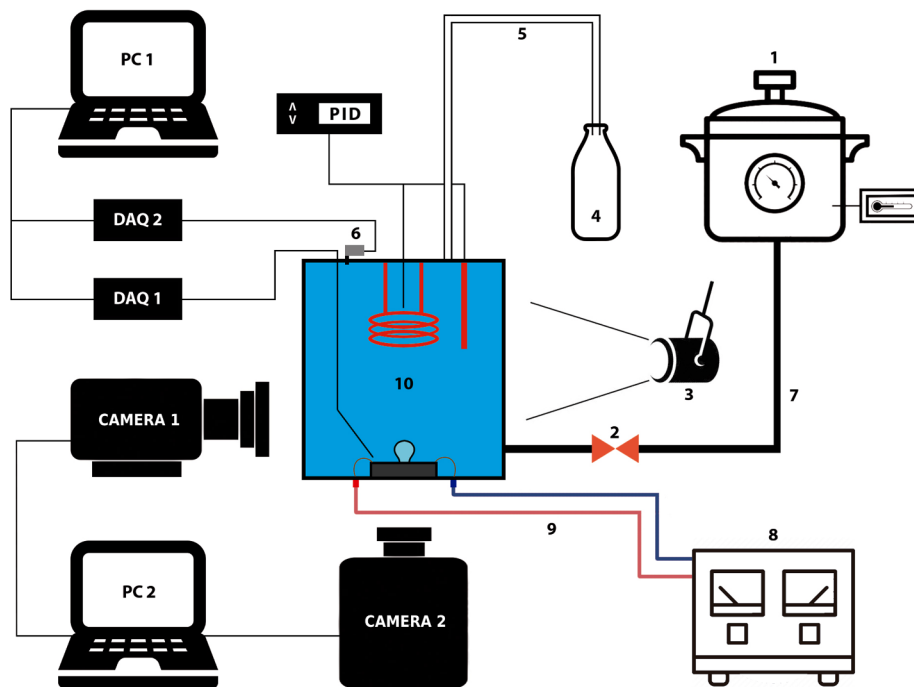


Fig. 1. Schematic representation of the experimental setup: (1) Degasification station, (2) Valve, (3) LED, (4) Condensate container, (5) Vapor outlet tube, (6) Pressure transducer, (7) Inlet water tube, (8) DC Power Supply, (9) Electrical cables, (10) Main tank.

2.2. Surface preparation

Several biphilic configurations were prepared for testing, according to the following steps:

1. A stainless-steel sheet (AISI304) with a thickness of 20 μm was cut to a defined dimension (50 \times 38 mm);
2. Two small steel blocks were duly sanded, cleaned and then welded to two copper wires;
3. A thin layer of silicone was placed on the upper face of a piece of thermal glass where the test surface was glued;
4. The free ends of the copper wires were fixed to an electrical connector, that was properly isolated from the stainless-steel base of the vessel with ceramic washers;
5. Several masks were prepared using PVC tape strips. In these tapes multiple patterns were made with one, two or three holes, with well-defined diameters and distances between them;
6. The selected strip was placed on the stainless-steel surface and several layers of a superhydrophobic spray (Neverwet-RustOleum) were deposited on the strip. This previously prepared PVC strip thus served as a stencil to prepare the biphilic patterns;
7. After 12 h of spraying the last layer, the PVC tape was removed revealing one or more well-defined superhydrophobic circular areas.

In the tested configurations, the diameter of the superhydrophobic regions was varied: $\varnothing = \{1.5 \text{ mm}; 2.4 \text{ mm}; 5.2 \text{ mm}\}$. In the biphilic configurations where the interactions between two bubbles were analysed, the distance between the regions was varied as follows: $d_{\text{spot}} = \{0.5\varnothing; 1\varnothing; 2\varnothing\}$. In the latter case, the value of the diameter for the superhydrophobic region was fixed to a single value, which was selected after the analysis of single bubble dynamics. For the configuration with three superhydrophobic regions both \varnothing and δ have already been defined, based on the previous parametric analysis of the size and distance between the superhydrophobic regions.

2.3. Characterization of the surfaces

The biphilic surfaces used in this work were characterized in terms of wettability and topography, as described in the following paragraphs. The wettability is quantified by measuring the static (θ_s) quasi-static advancing (θ_a) and receding (θ_r) contact angles and the hysteresis ($\Delta\theta$), as depicted in Table 1. The static angles were measured with an optical tensiometer (THETA-Attension), using the sessil drop method, as described in Pereira et al. [12], Moita et al. [10].

To obtain the quasi-static advancing angles a droplet was deposited on the surface and then slowly inflated. The first measurement of the angle was recorded when the liquid-solid contact line moved. The quasi-static receding angle was measured following the same procedure, but by withdrawing volume from the droplet and waiting for the retraction of the contact line. The hysteresis is given by the difference between θ_a and θ_r . The values obtained show that the areas covered by the coating have a superhydrophobic (SHF) behaviour ($\theta_s > 150^\circ$ and $\Delta\theta 10^\circ$). Consistently, the hydrophilic areas have contact angles ($\theta_s < 90^\circ$). The topography in the superhydrophobic regions was stochastic and was analysed using a Dektak3-Veeco profilometer, with a maximum vertical resolution of 200 \AA . A diamond probe was placed and dragged along the test surface, thus measuring the roughness profile. The obtained profiles were then processed to obtain the values of the mean roughness (R_a) and of the mean peak-to-peak roughness (R_z), which is the average of the highest peaks measured in one scan,

Table 1
Surface wettability measurements, using the optical tensiometer with the calculated Standard Deviation (SD).

Surface Wettability	θ_s [°] (SD)	θ_a [°] (SD)	θ_r [°] (SD)	$\Delta\theta$ [°] (SD)
Superhydrophobic	162.8 (2.7)	162.0 (3.7)	159.0 (4.2)	3.0 (8.0)
Hydrophilic	64.2 (0.7)	76.7 (2.5)	34.4 (5.3)	42.3 (4.5)

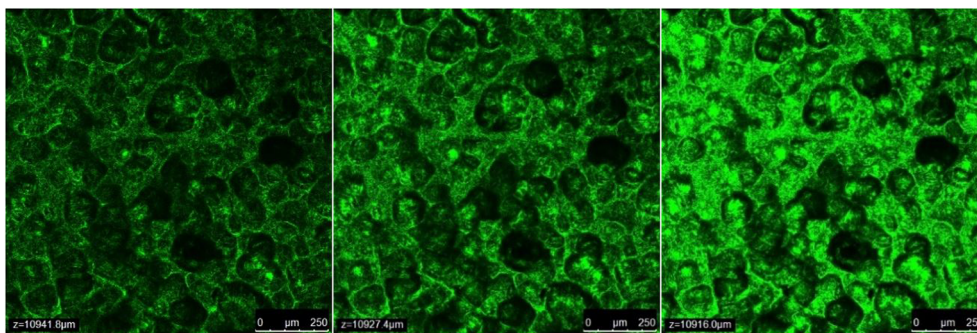


Fig. 2. Surface topography of the superhydrophobic regions, taken by confocal microscopy.

calculated according to standard DIN4768. At least five measurements were performed where $R_a = 5.8 \mu\text{m}$, with a standard deviation of $1.5 \mu\text{m}$, and $R_z = 22.6 \mu\text{m}$ with a standard deviation $3.9 \mu\text{m}$. The values of R_a and R_z for the hydrophilic areas were recorded as zero within the resolution of the equipment, whereby the roughness of these regions is negligible. To complement the information provided by the profilometer, a qualitative analysis of surface topography was also performed, with a Leica SP8 Confocal Microscope, used in the reflection mode. Based on the images obtained from this device it is possible to confirm the regularity in the topography of the superhydrophobic region. The images extracted can be seen in Fig. 2.

More details on the superhydrophobic coating have been obtained using a scanning electron microscope (SEM) FEI-QUANTA 200FEG operated in high vacuum mode at 20 kV. The images were captured by a BackScattered Electron Detector (BSED), Everhart-Thornley Detector (ETD) and in a combined mode of BSED and ETD labeled as (- - -).

As SEM analysis revealed (see Fig. 3 top row) the whole coating is covered by typical plastic shrinkage cracks which are formed during the coating’s drying process and were not observed by confocal microscopy. However, similar “cavity-like” irregularities shown by confocal microscopy were also detected by SEM in a combined BSED/ETD mode (see Fig. 3 top-right). At higher magnification near by the edges of the islands of superhydrophobic coating another “sponge-like” type of irregularities can be clearly seen on the surface of the coating (see Fig. 3 middle and bottom rows). Thus, it was found that the coating has a complex trimodal irregular structure which consists of cracks (around 30–500 μm in length and 2–40 μm in width) and cavities (around 2–90 μm in diameter) which are covered by a “sponge-like” mesh having pores (on the order of 5–75 nm in diameter). Obviously, such hierarchical structure helps to create superhydrophobicity.

The thickness of the superhydrophobic coating was also estimated from the SEM images. The specimen for the cross-sectional

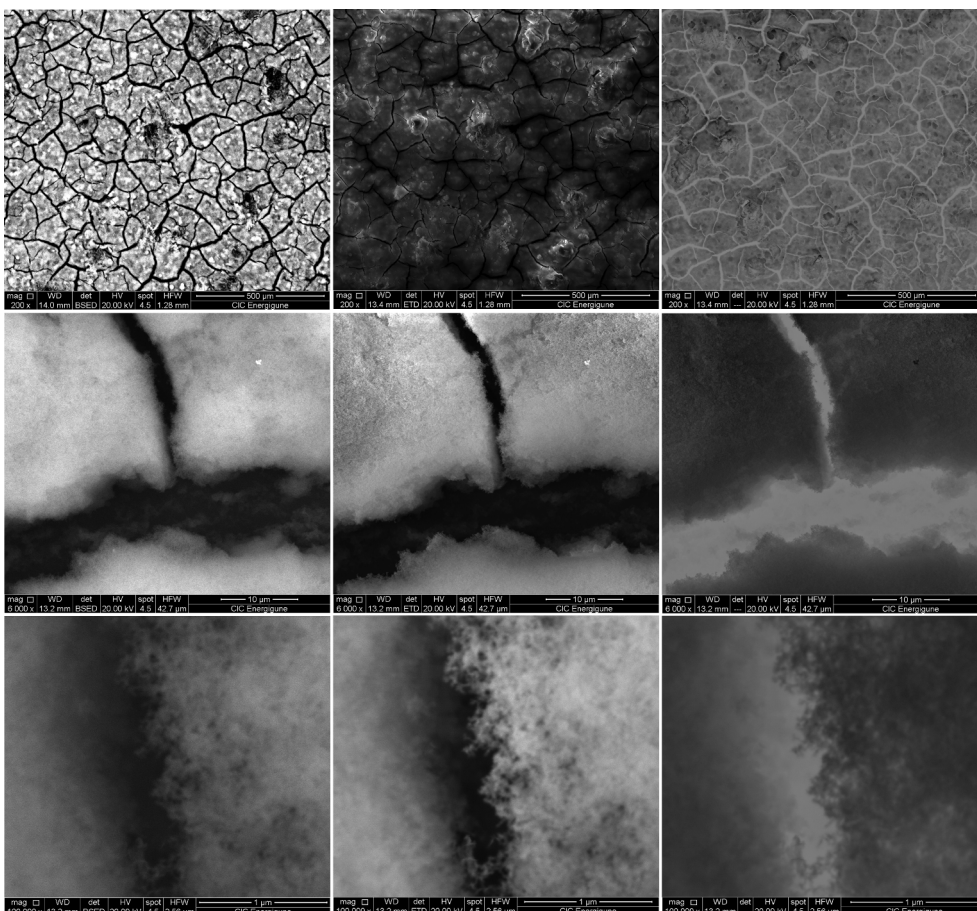


Fig. 3. Top view of the used superhydrophobic coating obtained by SEM at different magnifications: left column BSED; middle column ETD; right column BSED/ETD.

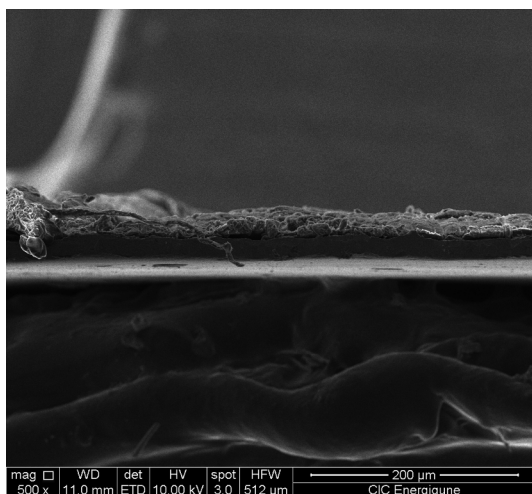


Fig. 4. Cross-sectional view of the used superhydrophobic coating obtained by SEM using an ETD detector.

characterisation was quenched in a liquid nitrogen for 30 s and once cryogenized, a blade was used for obtaining an accurate profile of the edge. After this procedure, the specimen was attached on a 90° cross section classical SEM holder and glued with double side carbon tape. The obtained image is shown in the Fig. 4. As can be seen, the thickness of the coating is $26 \pm 5 \mu\text{m}$.

Finally, it is worth mentioning the durability of the coating to assure the reproducibility of the measurements. The contact angles were measured before and after each boiling test for every surface tested. While the contact angle in the hydrophilic region was mainly kept unchanged, there was a reduction in the static contact angle of 5–10° in average in the superhydrophobic regions, after the boiling tests. However, contact angle hysteresis was always kept below 10°. Hence superhydrophobic properties were kept during the tests. Nonetheless, new surfaces were manufactured and characterized for each experiment.

2.4. Pool boiling tests

The experimental conditions imposed during the tests inside the main tank were continuously monitored and recorded, namely, a saturation temperature of $373.5 \pm 0.3 \text{ K}$, measured near the test surface, a pressure of $1000 \pm 10 \text{ mbar}$ and an adjustable heat flux on that same surface. Four different current intensity values were chosen to be imposed on the test surface: $I = \{3A; 5A; 7A; 9A\}$, corresponding to four different heat flux values: $q'' = \{0.03 \text{ W/cm}^2; 0.07 \text{ W/cm}^2; 0.13 \text{ W/cm}^2; 0.22 \text{ W/cm}^2\}$. It is worth mentioning that these heat flux values are not representative of the actual heat flux that triggers the nucleation site. This value corresponds to the power dissipated in the foil (calculated both theoretically with the resistance of the foil and experimentally, based on measurements of current and voltage). The dissipated power is then divided by the total area, thus providing a global average heat flux. However, the heat flux in the superhydrophobic region (as measured by the IR camera video analysis) is around 2–5 KW/m², which is in line with the values reported in the most recent studies on superhydrophobic surfaces, e.g. Teodori et al. [18].

The high-speed camera collected images for two different types of experiments. Long-term tests (20 min) to measure the bubble departure frequency for the different biphilic configurations and for the four different heat fluxes values. For these tests the number of bubbles that departed from the surface in a time period of 40.5 s were counted, for every 2 min, during 20 min. The period used was defined based on the maximum recording time of the high-speed camera within the used settings. The other test consisted of recording short videos, at 2200

Table 2

Uncertainty of the bubble dynamics parameters, measured for each SHF region diameter.

SHF region diameter	$e[d_{max}](\%)$	$e[\theta_{min}](\%)$
$\varnothing = 1.5 \text{ mm}$	7.8	26.5
$\varnothing = 2.6 \text{ mm}$	4.8	12.9
$\varnothing = 5.2 \text{ mm}$	7.8	10.6

Table 3

Uncertainty of the mean of the bubble departure frequencies, measured for each SHF region diameter and for each current intensity measurement.

SHF region diameter	$e[f_{3A}](\%)$	$e[f_{5A}](\%)$	$e[f_{7A}](\%)$	$e[f_{9A}](\%)$
$\varnothing = 1.5 \text{ mm}$	25.7	15.1	30.3	22.9
$\varnothing = 2.6 \text{ mm}$	13.2	17.9	20.1	24.3
$\varnothing = 5.2 \text{ mm}$	–	25.5	16.4	10.1

frames/s and lasting up to 6 s, in order to infer on the bubble dynamics history. These tests were also performed for the aforementioned four different imposed heat flux values. Thermographic videos of the stainless-steel sheet's bottom surface were recorded with the IR camera, lasting approximately 10 s. These videos showed clearly the temperature distribution map of the surface, associated to the boiling process. The stainless-steel sheet's bottom surface was black matt painted to place its emissivity near 1 (0.96) and minimize reflection issues. IR videos were synchronized with high-speed videos at an acquisition rate of (≈ 1600 frames/s), to obtain synchronized data on the heat transfer and bubble dynamics processes. A low integration time (200 μm) was used to obtain more information in the desired temperature range, although slightly increasing image noise. The size of the pixel depends on the optical arrangement used. For the cases considered here, the best pixel size was 100 μm for the IR arrangement and 50 μm for the high-speed arrangement. In both cases, MATLAB algorithms, developed and detailed in previous work [17], were used to process the thermographic and bubble dynamics images, respectively.

2.5. Uncertainties

Table 2 shows the maximum relative errors associated with the bubble dynamics parameters for biphilic configurations with three different SHF areas, with $q'' = 0.22 \text{ W/cm}^2$. The parameter d_{max} refers to the maximum bubble diameter and θ_{min} represents the minimum dynamic contact angle.

Table 3 shows the relative errors associated to the mean bubble departure frequency (f) measured for each biphilic configuration with one superhydrophobic region and for four different current intensity values. The data presented serves as reference for other tests performed with multiple superhydrophobic regions.

3. Results

3.1. Influence of the size of the superhydrophobic regions

The first tests were performed to infer on the influence of the superhydrophobic area in bubble dynamics and particularly bubble departure frequency. A first look at the temporal evolution of bubble growth, as depicted in Fig. 5 reveals a distinct behaviour related to the size of the superhydrophobic regions. Different stages of bubble formation, growth and detachment can be related to the size of the superhydrophobic region, in agreement with the detailed analysis reported in our previous work Pontes, Cautela, Teodori, Liu, Moita and Moreira [13], Pontes, Cautela, Teodori, Moita and Moreira [14]. Indeed, as detailed in these previous studies, bubble diameter is constrained by the size of the hydrophobic area, growing up to the limit of

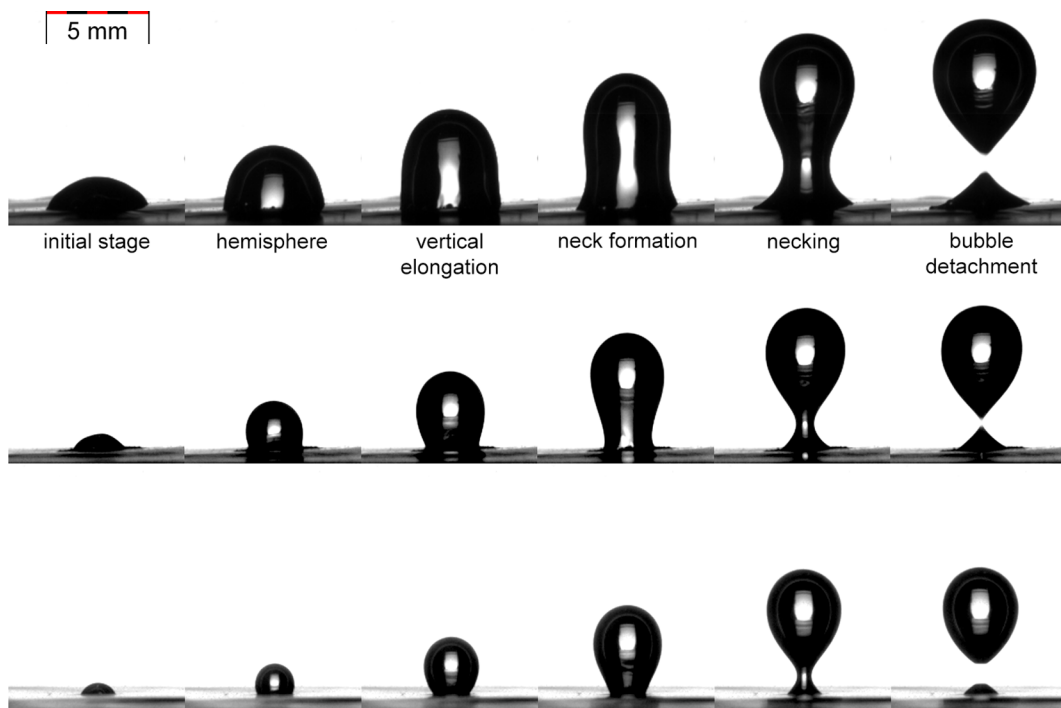


Fig. 5. Dynamic analysis of bubble growth and detachment for the 3 studied superhydrophobic region sizes. From top to bottom: $\varnothing = 5$ mm, $\varnothing = 2.4$ mm, $\varnothing = 1.5$ mm.

the boundaries between the superhydrophobic region and the remaining hydrophilic surface. Since there is no surface tension component, in the superhydrophobic region contributing to the detachment of the bubble, surface tension acts mainly at the boundary of the superhydrophobic region. Hence, for smaller superhydrophobic areas, the necking is promoted so that departure frequency is slightly increased. In any case, generally the necking occurs at latter stages of bubble growth, when compared to hydrophilic or even to hydrophobic surfaces and as the bubble detaches, the superhydrophobic region is immediately covered by a new vapour layer, so contrarily to observations reported in the literature using such surfaces, there is no quenching associated to liquid rewetting on superhydrophobic regions. However, the liquid in the hydrophilic region may flow, being promoted through bubble departure and coalescence. In this context, particular interest arises from the analysis of bubble departure diameter and frequency as a function of the diameter of the superhydrophobic area. As aforementioned, the geometry of the superhydrophobic area will affect bubble departure

size and frequency, which also affect directly the estimation of the heat flux term associated to the latent heat of evaporation. Also, bubble departure frequency and diameter depend on the force balance between adhesive forces related to surface tension at the boundary of the superhydrophobic area and the buoyancy forces, which again are associated to the size of the superhydrophobic region, which in turn may affect interaction/coalescence phenomena, thus contributing to the latent heat term and to the induced convection.

From a post-processing algorithm, it is possible to obtain the detachment diameter. These values were later compared with the base diameter, as shown in Fig. 6(a). In this plot, the detachment diameter is compared to the base diameter. The plot shows an evident trend: the smaller the diameter of the superhydrophobic area the larger it is the ratio between the detached bubble diameter and the base diameter. Regarding the departure frequency, as depicted in Fig. 6(b) the results show that smaller superhydrophobic regions promote larger frequencies, reaching around 2 Hz for a heat flux of 0.218 W/cm². This

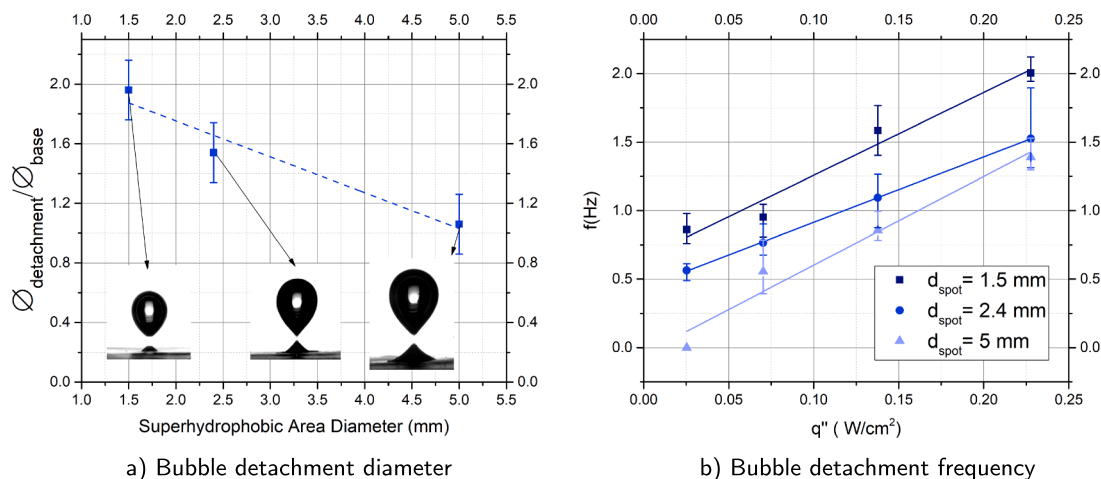


Fig. 6. Effect of the diameter of the superhydrophobic areas in bubble dynamic parameters.

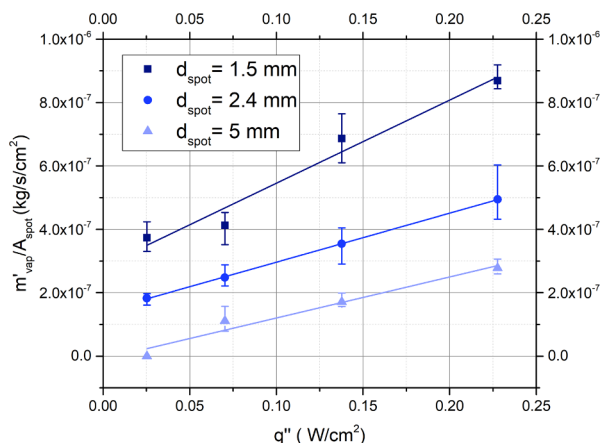


Fig. 7. Effect of the diameter of the superhydrophobic regions in bubble detachment evaporated mass flux ratio.

trend, which is in agreement with the larger departure diameter observed in the larger superhydrophobic areas, can be attributed to the fact that in these larger areas the surface tension forces only act in the boundary of the superhydrophobic region with the hydrophilic region. Hence, the bubble grows freely in the superhydrophobic area and the surface tension forces can also act at later growth stages, thus delaying bubble detachment. Also, the increase in the frequency with the heat flux is clear in all the cases.

The size of the superhydrophobic areas was also analyzed in terms of the resulting evaporated mass, which is directly related with the term of heat flux associated to the latent heat of evaporation. To infer which configuration allows for a better use of the superhydrophobic areas, maximizing the evaporated mass and consequently the term of heat flux removed by latent heat, this quantity was divided by the area occupied by the superhydrophobic region (Fig. 7). Therefore, this Figure shows the ratio between the vapour flux and the base area of the superhydrophobic region. Based on this representation it is possible to infer that the configuration with the smallest superhydrophobic areas is again better in promoting liquid evaporation, thus increasing the heat flux term associated to the latent heat. Therefore, the 1.5 mm diameter area was chosen to analyze, in the next section, the effect of the distance between two of these superhydrophobic areas on the heat transfer performance of the surface. Smaller diameters were not analyzed due to constraints in the manufacturing process currently used to produce the superhydrophobic areas, but the diameter of 1.5 mm was used in further testing of the ideal distance between superhydrophobic areas.

3.2. Effect of the distance between superhydrophobic regions

The distance between superhydrophobic regions was analyzed for 3 distances, namely $0.5 \varnothing_{base}$, $1 \varnothing_{base}$ and $2 \varnothing_{base}$. Illustrative images of bubble dynamics for each of these distances are provided in Fig. 8. In the first case, i.e. for the smallest distance between superhydrophobic regions, the bubbles clearly interact. Later they coalesce, forming a bridge between the vapour layers, thus insulating the surface between the areas.

Frequency measurements were taken for all of these cases, for one of the superhydrophobic areas, for the four different heat fluxes, as considered in the previous analysis. The case of the smallest distance between superhydrophobic areas ($0.5 \varnothing_{base}$) was not considered here, as the proper evaluation of the detachment frequencies became very hard due to coalescence, as illustrated in Fig. 9.

As aforementioned, the bubbles formed in two adjacent superhydrophobic areas with a distance smaller than the diameter of the bubbles, coalesce and form a bridge of vapor that insulates the surface. This can be observed, not only in the high-speed images but also in thermographic images, as illustrated in the image to the right in Fig. 9. The hotter region in the center (in yellow) represents the vapour covered area. The cold region in the surroundings represents the area where evaporation is occurring. So, if this distance was adopted and the pattern applied to a surface, vapour would cover it entirely, the entirety of it, insulating the surface and decreasing the heat flux. Hence, this case will be disregarded for the rest of the analysis.

The frequency obtained for the superhydrophobic areas separated by the two other distances of $1 \varnothing_{base}$ and $2 \varnothing_{base}$ is depicted in Fig. 10(a) along with the single bubble case, for comparative purposes. The Figure evidences a similar behaviour in both cases, suggesting that there is no considerable effect of the distance between areas in these cases. The results obtained for the largest distance between superhydrophobic areas are similar to those obtained for a single bubble, since there is no interaction between the superhydrophobic sites. On the other hand, for the case where the distance is equal to the diameter of the superhydrophobic area, and therefore is similar to the bubble diameter, the departure frequency is slightly lower, probably due to the interaction between bubbles and sites. This does not necessarily lower the efficiency of the surface. In fact as discussed in the previous paragraphs, a mild coalescence may promote the fluid flow in the hydrophilic region, between superhydrophobic areas, thus actually facilitating the heat transfer from the surface to the liquid. Such beneficial effect is actually confirmed in the thermographic images, thus suggesting an effective promotion of the cooling effect for this distance between superhydrophobic regions of about one diameter of the bubbles. On the other hand, evaluating again the evaporated mass, the results clearly show that although the departure frequency increases for the largest difference between the superhydrophobic areas, since the interaction between bubbles, which delays the departure frequency as it promotes bubbles' coalescence, is precluded, does not favour the mass evaporation. On the contrary, the analysis performed here, as depicted in Fig. 10 b), which considered, not only the superhydrophobic coated areas but also the non-coated area between the two bubbles clearly shows that the evaporated mass flux ratio is in fact lower for the largest distance between superhydrophobic areas. This implies that there is no advantage in distancing the areas to avoid the interference between superhydrophobic areas. On the other hand, the interference must be controlled spacing the regions with a distance of about the size of the diameter of the bubbles (which in turn is close to that of the bubbles as they grow within the entire superhydrophobic region, constrained by the boundaries with the hydrophilic regions) seems to promote a positive bubble interaction, which in turn, favours the liquid motion between the bubbles and the surface, favouring the surface cooling.

These trends are however better understood, as one relates bubble dynamics with the information taken from the thermographic images,



Fig. 8. Comparison between several tested distances between the superhydrophobic areas. From left to right: $0.5 \varnothing_{base}$, $1 \varnothing_{base}$ and $2 \varnothing_{base}$.

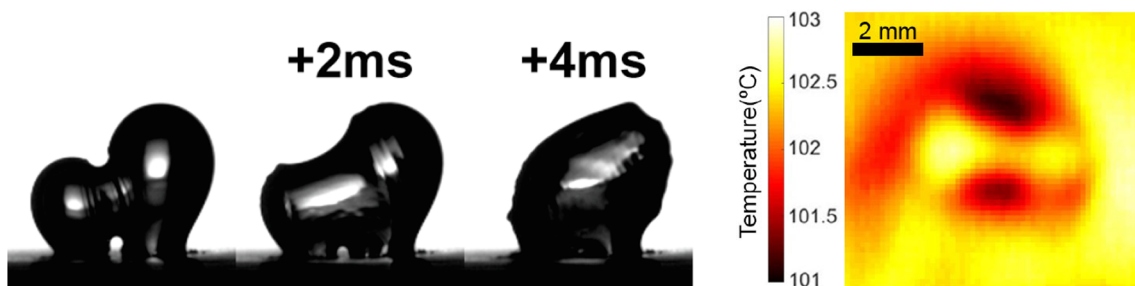


Fig. 9. Coalescence phenomena depicted for the $0.5\varnothing_{base}$ case. High-speed and thermographic images.

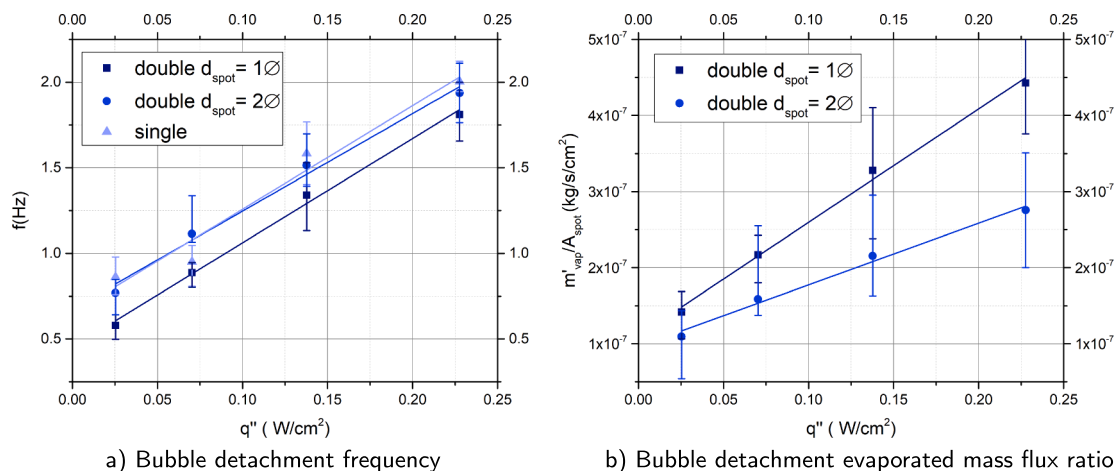


Fig. 10. Comparison of frequency and evaporated mass between different distances separating the superhydrophobic regions.

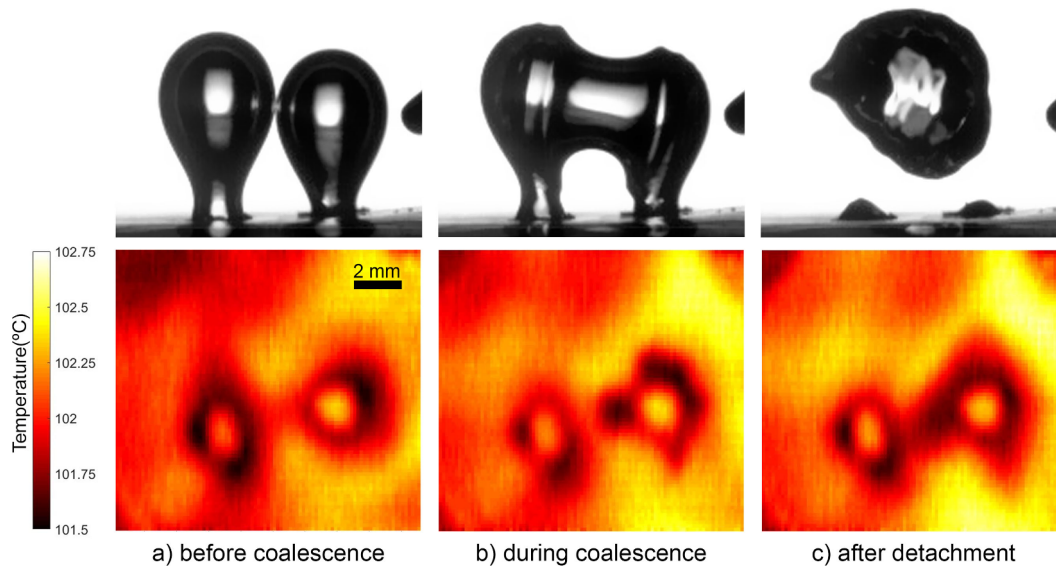


Fig. 11. Thermographical analysis of bubble nucleation and interaction with a distance of $1\varnothing$ between superhydrophobic regions.

which were synchronized with those of the high-speed camera. Looking at the thermographic images taken for the case which led to the best results in terms of evaporated mass. i.e., $1\varnothing$, in Fig. 11, one may relate in detail the bubbles' growth and departure processes and the surface temperature fields. Exactly before bubble detachment, as represented in Fig. 11b, there is a drop in the surface temperature, in the centre region, between the two bubbles. This is consistently observed throughout

several instances of bubble detachment during the experiment. This confirms that a controlled bubble interaction can somehow be advantageous, creating a periodic induced flow between superhydrophobic regions, that cools the surface.

This flow is more pronounced in the surface with 3 superhydrophobic areas, as discussed in the following sub-section.



Fig. 12. High speed images of bubble detachment and coalescence of the surface with multiple superhydrophobic regions.

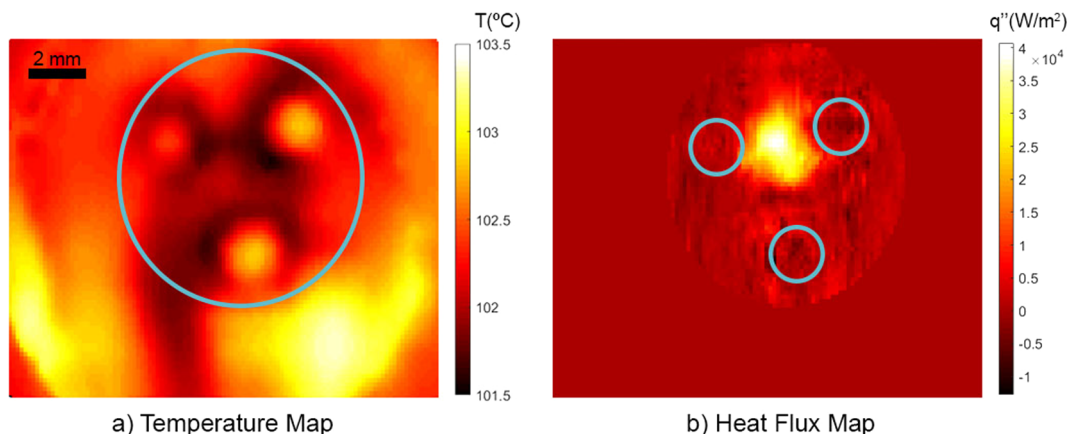


Fig. 13. Thermographical images of bubble detachment (a) and Heat flux (b) for a surface with three superhydrophobic regions. The 1 mm diameter superhydrophobic areas are equally spaced by the distance of one diameter.

3.3. High-Speed and Thermographic analysis of the pattern influence on heat transfer

As stated in the experimental procedure section, the thermographic data was extracted in sync with the high-speed images. A final analysis on the effect of the pattern was therefore performed, taking advantage of this synchronization, to better relate the bubble dynamic processes with the temperature fields obtained on the surface. For this, the distance of 1 diameter between superhydrophobic areas, using the areas with the smallest diameter, was chosen to develop the pattern on the stainless steel foil, in agreement with the analysis of the results performed so far. This pattern is therefore composed by 3 equidistant superhydrophobic areas, creating 3 distinct nucleation regions, as shown in Fig. 12. Similarly to what was observed in the surface with 2 areas in Figs. 9 and 11, coalescence occurs during bubble detachment, but vapour does not occupy the entire surface, but instead, it clearly allows for some liquid to recirculate in the hydrophilic surface, thus promoting high heat fluxes to be extracted. Also, the coalescence of the bubbles promotes flow circulation and convection heat transfer.

In this final configuration, the heat flux was studied through thermography. The measured temperature field can be seen on the left in Fig. 13a). Here one may identify 3 different “hot spots” that correspond to the superhydrophobic areas. The blue circle represents the selected area, used to calculate the heat flux. The area surrounding the superhydrophobic regions shows lower temperatures, while the superhydrophobic areas form the highest temperatures. One can also clearly observe that the surface temperature is lower in the boundary regions of the “hot spots” than in the rest of the surface, i.e. in the boundary of the superhydrophobic regions.

The heat flux was derived from the temperature map given by the thermographic camera, using a post processing algorithm developed in house, on MATLAB. This was done by applying a pixel by pixel energy

balance on the stainless steel foil. This energy balance is described by Eq. (1). In this equation q'' is the flux in the analysed pixel, q_0'' is heat flux released by the heated foil, k_h , ρ_h and $c_{p,h}$ are the conductivity, density and specific heat capacity of the heater’s material and δ_h is the thickness of the heater. Here three main terms can be distinguished, namely the initial heat flux supplied, the heat flux spread through the foil (the spatial component) and the measured time variation of the temperature.

$$q'' = q_0'' + k_h \delta_h \left(\frac{\partial^2 T}{\partial x^2} + \frac{\partial^2 T}{\partial y^2} \right) - \rho_h c_{p,h} \delta_h \frac{\partial T}{\partial t} \quad [W/m^2] \quad (1)$$

After applying the post processing algorithm, the heat flux images are also extracted and analysed. In this context, Fig. 13(b) illustrates an example of the heat flux obtained during the process of bubble growth. A peak in the heat flux is represented here by the lighter colored region of the figure. In blue, the small circles represent the superhydrophobic areas. Due to the flow induced by bubble departure, a peak of heat flux occurs in the region of the surfaces corresponding to the center of the bubbles formed in the superhydrophobic areas. The overall dissipated power is calculated by integrating the heat flux points in the selected area. For a better analysis of this phenomenon, the dissipated power in the blue circular region and the heat flux in the center of this particular circle where plotted against the bubble departure events, detected in the synchronized high speed videos. The results are presented in Fig. 14. The blue data points depict the Dissipated Power in the region, and the values can be read in the axis to the right. The black data points are representative of the local heat flux in the central point of the region and the values can be read in the left axis. The green vertical lines are the bubble departures detected in the high-speed images, which are synchronized with the thermographic images. The surface geometry is the same considered in Fig. 13.

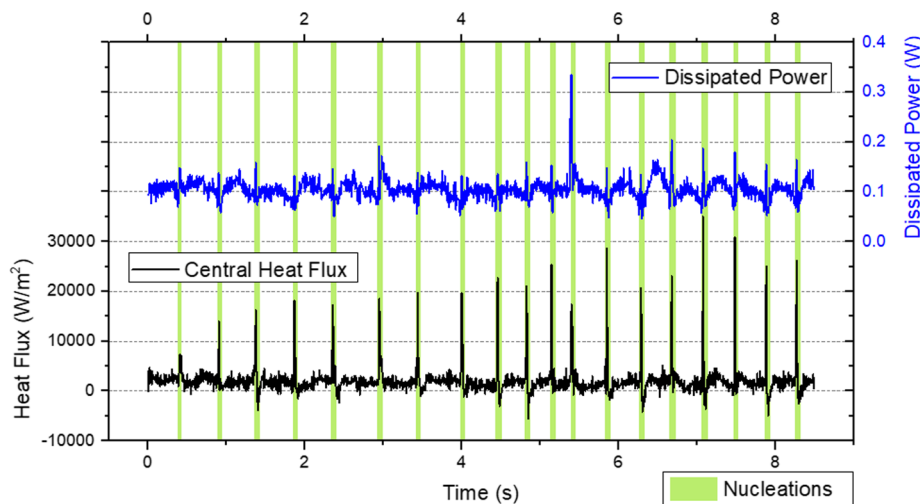


Fig. 14. Measured heat flux and dissipated power during boiling for the stainless steel foil with 3 superhydrophobic regions of 1 mm, equally distanced at 1 bubble diameter. The green lines represent the bubble departure events that were detected in the high-speed images synchronized with the thermographic images. (For interpretation of the references to colour in this figure legend, the reader is referred to the web version of this article.)

In this Figure it is possible to see several peaks in both graphs, which perfectly coincide with the bubble departure events in the superhydrophobic areas, thus proving the heat transfer enhancement due to the use of the biphilic surface with this geometry. These results further suggest that the method used here to define the geometric pattern of the biphilic surface, although requiring improvements, is a tool to define a systematic and objective way to obtain the biphilic patterns, decreasing the use of a trial-and-error approach.

4. Conclusions

This paper assessed the effect of the size of superhydrophobic regions and the distance between adjacent regions in biphilic surfaces, focusing on single events. It can be concluded that surfaces with smaller superhydrophobic regions led to the formation and detachment of bubbles with a higher frequency. By extrapolating the frequency and multiplying by the volume of detached vapour, the evaporated mass flow rate, which is directly related to the latent heat term removed from the heated surface, was calculated and proved also higher when considering the use of patterns with smaller superhydrophobic areas.

To evaluate the effect of the distance between superhydrophobic regions, three additional biphilic configurations were selected, with two superhydrophobic regions and a variable spacing between regions of: $\delta \approx \{0.5\phi, 1\phi, 2\phi\}$. Promising results are achieved for the 1ϕ configuration, that enables moderate coalescence between detaching bubbles. The coalesced bubbles are larger and consequently decrease the bubble departure frequency from the superhydrophobic areas, when compared to the case of a single bubble generation. However, the synchronized high-speed video and thermal images show that this coalescence promotes a convective flow of the liquid between the superhydrophobic areas, which causes a visible drop in the surface temperature. The evaporated mass flux is also larger for this distance between superhydrophobic regions, which is in turn also associated to a larger heat flux removed by latent heat.

Based on these results an “optimum” biphilic pattern was devised using three superhydrophobic areas. Post processing of the thermal data allowed evaluating the heat flux that is removed from the surface for this scenario. The results show an evident relation between bubble departure events from the superhydrophobic areas and a peak in the heat flux in the surrounding surface region, thus confirming the enhancement in the heat transfer promoted by the use of the biphilic patterns. Furthermore, these results also indicate that the method used here to define the geometric pattern of the biphilic surface, can be used as a tool to define a systematic and objective way to obtain the biphilic patterns, decreasing the use of a trial-and-error approach.

Declaration of Competing Interest

The authors declare that they have no known competing financial interests or personal relationships that could have appeared to influence the work reported in this paper.

Acknowledgements

Authors are grateful to Fundacao para a Ciencia e Tecnologia (FCT) for partially financing the research under the framework of the project JICAM/0003/2017, which also provided support with a fellowship. Authors also acknowledge FCT for the IF 2015 recruitment program (IF 00810–2015) and exploratory project associated with this contract. Finally the authors thank Universidade de Lisboa, for providing a scholarship to Pedro Pontes.

References

- [1] A.R. Betz, J. Jenkins, D. Attinger, et al., Boiling heat transfer on superhydrophilic, superhydrophobic, and superbiphilic surfaces, *Int. J. Heat Mass Transf.* 57 (2013) 733–741.
- [2] J. Buongiorno, D.G. Cahill, C.H. Hidrovo, S. Moghaddam, A.J. Schmidt, L. Shi, Micro- and nanoscale measurement methods for phase change heat transfer on planar and structured surfaces, *Nanoscale Microscale Thermophys. Eng.* 18 (2014) 270–287.
- [3] H. Jo, H.S. Ahn, S. Kang, M.H. Kim, A study of nucleate boiling heat transfer on hydrophilic, hydrophobic and heterogeneous wetting surfaces, *Int. J. Heat Mass Transf.* 54 (2011) 5643–5652.
- [4] H. Jo, H.S. Park, M.H. Kim, Single bubble dynamics on hydrophobic–hydrophilic mixed surfaces, *Int. J. Heat Mass Transf.* 93 (2016) 554–565.
- [5] H.J. Jo, H.M. Kim, H.S. Ahn, S.T. Kim, S.H. Kang, J.W. Kim, M.H. Kim, The nucleate boiling heat transfer by the hydrophobic milli-dot on the silicon surface, *Proceedings of the KNS spring meeting*, 2009.
- [6] D.E. Kim, D.I. Yu, D.W. Jerng, M.H. Kim, H.S. Ahn, Review of boiling heat transfer enhancement on micro/nanostructured surfaces, *Exp. Therm. Fluid Sci.* 66 (2015) 173–196.
- [7] C.S. Kumar, Y.W. Chang, P.H. Chen, Effect of heterogeneous wettable structures on pool boiling performance of cylindrical copper surfaces, *Appl. Therm. Eng.* 127 (2017) 1184–1193.
- [8] I. Malavasi, E. Teodori, A.S. Moita, A.L. Moreira, M. Marengo, Wettability effect on pool boiling: a review, *Encyclopedia Two-Phase Heat Transf. Flow III* (2018) 1–61.
- [9] A. Moita, E. Teodori, A. Moreira, Influence of surface topography in the boiling mechanisms, *Int. J. Heat Fluid Flow* 52 (2015) 50–63.
- [10] A.S. Moita, C. Laurência, J.A. Ramos, D.M.F. Prazeres, A.L.N. Moreira, Dynamics of droplets of biological fluids on smooth superhydrophobic surfaces under electrostatic actuation, *J. Bionic Eng.* 13 (2016) 220–234.
- [11] A.R. Motezakker, A.K. Sadaghiani, S. Çelik, T. Larsen, L.G. Villanueva, A. Koşar, Optimum ratio of hydrophobic to hydrophilic areas of biphilic surfaces in thermal fluid systems involving boiling, *Int. J. Heat Mass Transf.* 135 (2019) 164–174.
- [12] P.M.M. Pereira, A.S. Moita, G.A. Monteiro, D.M.F. Prazeres, Characterization of the topography and wettability of english weed leaves and biomimetic replicas, *J. Bionic Eng.* 11 (2014) 346–359.
- [13] P. Pontes, R. Cautela, E. Teodori, Y. Liu, A.S. Moita, A. Moreira, 2019. Effect of pattern geometry on bubble dynamics and heat transfer on biphilic surfaces, in: 14th International Conference on Heat Transfer, Fluid Mechanics and Thermodynamics, HEFAT.
- [14] P. Pontes, R. Cautela, E. Teodori, A.S. Moita, A. Moreira, 2019. Bubble dynamics and heat transfer on biphilic surfaces, in: 10th International Conference on Multiphase Flow, ICMPF.
- [15] A.K. Sadaghiani, R. Altay, H. Noh, H. Kwak, K. Şendur, B. Misirlioğlu, H. Park, A. Koşar, Effects of bubble coalescence on pool boiling heat transfer and critical heat flux—a

- parametric study based on artificial cavity geometry and surface wettability, *Int. J. Heat Mass Transf.* 147 (2020) 118952.
- [16] A. Sialaff, J. Dietl, S. Herbert, P. Stephan, The influence of system pressure on bubble coalescence in nucleate boiling, *Heat Transfer Eng.* 35 (2014) 420–429.
- [17] E. Teodori, P. Pontes, A. Moita, A. Moreira, Thermographic analysis of interfacial heat transfer mechanisms on droplet/wall interactions with high temporal and spatial resolution, *Exp. Therm. Fluid Sci.* 96 (2018) 284–294.
- [18] E. Teodori, T. Valente, I. Malavasi, A. Moita, M. Marengo, A. Moreira, Effect of extreme wetting scenarios on pool boiling conditions, *Appl. Therm. Eng.* 115 (2017) 1424–1437.
- [19] M. Yamada, B. Shen, T. Imamura, S. Hidaka, M. Kohno, K. Takahashi, Y. Takata, Enhancement of boiling heat transfer under sub-atmospheric pressures using biphilic surfaces, *Int. J. Heat Mass Transf.* 115 (2017) 753–762.
- [20] M. Zupančič, M. Može, P. Gregorčič, A. Sitar, I. Golobič, Evaluation of enhanced nucleate boiling performance through wall-temperature distributions on pdms-silica coated and non-coated laser textured stainless steel surfaces, *Int. J. Heat Mass Transf.* 111 (2017) 419–428.